Chapter 8
Microwave Antenna Holography

David J. Rochblatt

8.1 Introduction

The National Aeronautics and Space Administration (NASA)–Jet Propulsion Laboratory (JPL) Deep Space Network (DSN) of large reflector antennas is subject to continuous demands for improved signal reception sensitivity, as well as increased transmitting power, dynamic range, navigational accuracy, and frequency stability. In addition, once-in-a-lifetime science opportunities have increased requirements on the DSN performance reliability, while needs for reduction of operational costs and increased automation have created more demands for the development of user friendly instruments. The increase in the antenna operational frequencies to X-band (8.45 gigahertz (GHz)) and Ka-band (32 GHz), for both telemetry and radio science, proportionately increased the requirements of the antenna calibration accuracy and precision. These include the root-mean-square (rms) of the main reflector surface, subreflector alignment, pointing, and amplitude and phase stability. As an example, for an adequate performance of an antenna at a given frequency, it is required that the reflector surface rms accuracy be approximately $\lambda/20$ (0.46 millimeter (mm) at Ka-band) and that the mean radial error (MRE) pointing accuracy be approximately $\lambda/(10*D)$, or a tenth of the beamwidth (1.6 millidegrees (mdeg) for a 34-meter (m) antenna at Ka-band).

Antenna microwave holography has been used to improve DSN performance. Microwave holography, as applied to reflector antennas, is a technique that utilizes the Fourier transform relation between the complex far-field radiation pattern of an antenna and the complex aperture distribution. Resulting aperture phase and amplitude-distribution data are used to precisely

characterize various crucial performance parameters, including panel alignment, subreflector position, antenna aperture illumination, directivity at various frequencies, and gravity deformation effects. The holography technique provides a methodology for analysis, evaluation, and radio-frequency (RF) performance improvement of large reflector and beam waveguide antennas. Strong continuous-wave (CW) signals can be obtained from geostationary satellites and used as far-field sources. Microwave holography has been one of the most economical techniques for increasing the performance of the large DSN antennas in terms of cost-to-performance ratio. This chapter describes the instrument design and the mathematical algorithms and software for the development of the holographic measurement system. In addition, it describes its application in the DSN to improve, optimize, and maintain its performance to prescribed specifications.

The word “holography” is derived from the Greek “holos,” which means “whole.” Therefore, a hologram is created when the whole information can be recorded and presented graphically. In the antenna engineering case, the whole information is the amplitude, frequency, and phase of the signal or the transfer function of the antenna. We know that in optics, when a hologram is created we can see the depth of the image, which is absent in regular camera images. The reason is that a camera records only the intensity (square amplitude) of light at a given frequency (for which the film is sensitive). In holographic recording, the phase is recorded in addition to the amplitude at a given frequency range. It is the recording of phase that contains the depth, or the third dimension, that gives it a life-like perception. Good painters know how to play with light and shadow to create the “feel” of depth in their painting. It is the recording of the phase in the antenna holography that enables us to derive the misalignment of the antenna panels in the direction perpendicular to the x-y plane or the z-axis.

To obtain a hologram of the entire antenna dish surface, a two-dimensional sampling of the antenna far-field pattern must be recorded. Holographic recording acquires the phase and amplitude information utilizing raster-scan patterns of the antenna angular response. (Note: raster scans are the most popular, although other scan geometries are possible and could be advantageous under certain conditions.) Holographic metrology is based on interferometrically connecting a reference antenna to the large test antenna and digitally recording the test antenna amplitude and phase response. This is done by continuously scanning the test antenna against a signal source from a geosynchronous satellite, following a two-dimensional grid (Fig. 8-1).

Celestial radio sources can also be used but require a different receiver architecture. Their usual lower signal strength imposes limitations and introduces additional complexity to the measurement and the data processing. Their sidereal motion across the sky would require a faster data acquisition to avoid smearing of the resulting surface map.

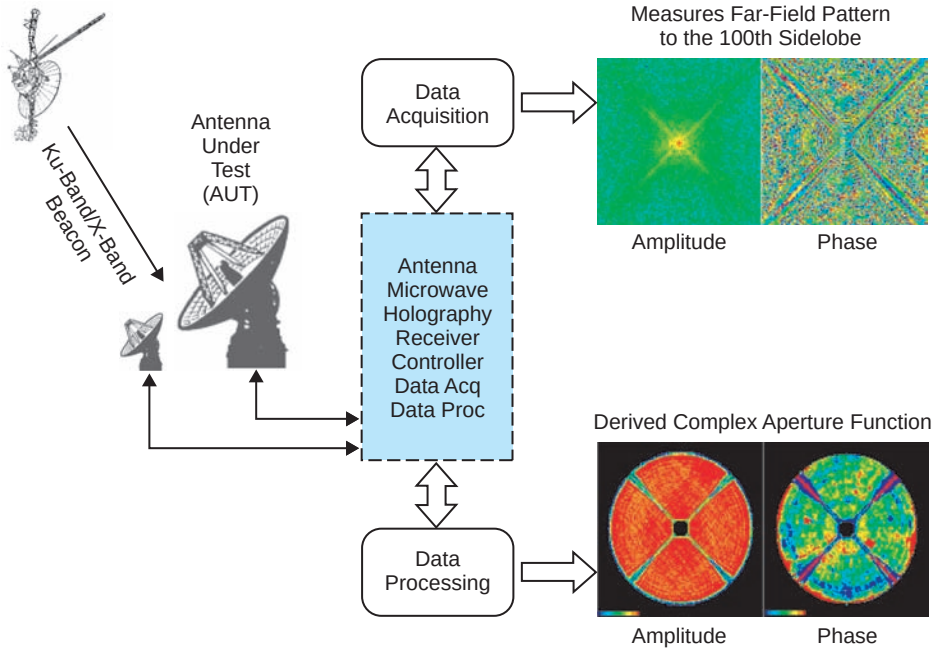

FIg. 8-1. Antenna microwave holography activities diagram.

When a regularized far-field grid can be measured, an inverse fast Fourier transform (FFT) algorithm can then be used to obtain the desired information, consisting of the test antenna aperture amplitude and phase response [1–6]. Other irregularized grids [7] can also be used for the measurements followed by other inversion techniques than the FFT (as an example, a singular value decomposition). The angular extent of the response that must be acquired is inversely proportional to the size of the desired resolution cell in the processed holographic maps. From the aperture phase response, the surface error map is calculated, and the amplitude response is directly displayed. The information in the surface error map is used to calculate the adjustments of the individual panels in an overall main reflector best-fit reference frame. The amplitude map provides valuable information about the energy distribution in the antenna aperture (Fig. 8-1).

The ultimate performance of a large, steerable, reflector antenna is limited by imperfections of the reflecting surface. The size of the panels that form the surface of the antenna and the allowable level of losses due to surface inaccuracies dictate the required resolution of the measurements. For a maximum of 0.1-decibel (dB) degradation in antenna efficiency due to surface imperfections, the rms surface error (ε) must be no greater than $0.012\,\lambda$ where λ is the wavelength of the operating antenna frequency. When the surface error

is $0.024\,\lambda$, degradation in antenna efficiency is 0.4 dB, which demonstrates the exponential relationship between surface error and gain loss.

For $\varepsilon/\lambda < 1/4\pi$, this relationship (also known as the Ruze formula) can be expressed [8]:

$$\frac{\eta_A}{\eta_0} = \exp-\left(\frac{4\pi\varepsilon}{\lambda}\right)^2 + \left(\frac{2r_o}{D}\right)\left[1-\exp-\left(\frac{4\pi\varepsilon}{\lambda}\right)^2\right] \qquad (8.1\text{-}1)$$

where,

η_A = efficiency of the physical antenna

η_0 = efficiency of a hypothetical antenna with absence of surface errors

ε = rms of surface deviation in the axial direction

λ = wavelength

r_o = correlation radius

D = antenna diameter

For totally random surface phase errors, $r_o = 0$, and the Ruze formula, Eq. (8.1-1) reduces to its first term. When r_o is significant relative to *D*, the second term in Eq. (8.1-1) adds to the first term to yield a higher efficiency value than in the case where the errors are totally random. Therefore, using the first term in Eq. (8.1-1) yields the worst-case value for a given surface rms value.

Figure 8-2 shows the gain loss of a reflector antenna (of any size) as a function of its rms surface error using Eq. (8.1-1) and assuming $r_o = 0$. As can be seen from this plot, reducing the reflector effective rms error from 0.67-mm to 0.25-mm will result in an antenna gain increase of 3.0 dB at Ka-Band (32 GHz). In the DSN, this indeed has been the case as most of the 34-m Beam

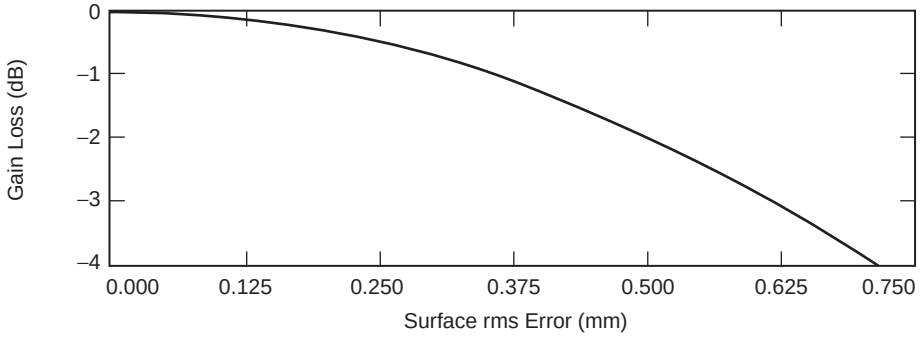

Fig. 8-2. Antenna gain loss versus rms surface error at 32 GHz.

Waveguide (BWG) antenna's panels were initially set by a theodolite technique and later refined by the holographic technique that improved their performances by 3 dB (on average).

Antenna microwave holography implementation typically has to meet several requirements. It must satisfy the requirements for a fast (45-minute) "health check" measurement, utilizing low-resolution medium-precision images to determine the antenna status. It also must provide high-resolution, high-precision images measured over a period of no longer than 12 hours to avoid thermal diurnal effects.

8.2 Holography System Simulation

Two approaches for the system architecture are typically used. These are based on a wide bandwidth or a narrow bandwidth receiver architecture. To facilitate the examination of either of the two approaches, we developed simulation algorithms.

The parameters critical for the quality of the images derived from holographic measurements are signal-to-noise ratio, maximum scan angle, instrumentation dynamic range, related approximations (may be included due to different sampling techniques) and overall system accuracy. A detailed mathematical derivation of the related equations can be found in [9,10]. In general, to derive the standard deviation in the final holographic map from simulation, we first compute the far-field pattern of the perfect reflector antenna. A simulation tool is developed by superimposing the contribution of the measurement system noise on the far-field patterns [9]. By processing the new far-field data and displaying the images, one can derive the standard deviation error in processed holographic maps. The NASA-DSN-JPL 64-m antennas prior to their upgrade to 70-m diameter [11] were used for the simulations case study. These three Cassegrain antennas (located at Goldstone, California; Robledo de Chavela, Spain; and Tidbinbilla, Australia) were designed with –13 dB amplitude aperture taper illumination. Prior to the upgrade of the three antennas to 70-m, these antennas had on average an rms surface error of 1.34-mm (details for each antenna are provided in Table 8-1). In the post 70-m upgrade, these antennas were all set holographically [12] to an average value of 0.65 mm, which improved their performance at X-band by approximately 0.75 dB.

Table 8-1. Holography historical data.

Antenna Diameter (m)	DSS*	Date	Meas. Freq. (GHz)	Resolution (m)	Elevation (deg)	Initial rms (mm)	Final rms (mm)	Gain Improvement (dB) Frequency Band S	X	Ka
70-m Antennas										
70	14	4/88	12.198	0.42	47.0	**1.26**	**0.64**	0.05	0.64	9.3
70	43	10/87	12.750	0.44	47.0	**1.18**	**0.65**	0.04	0.59	8.5
70	63	7/87	11.451	0.42	42.0	**1.58**	**0.65**	0.09	1.17	16.9
DSS-13 34-m R&D Antenna										
34	13	9/90	12.198	0.32	46.0	**0.88**	**0.43**	0.02	0.32	4.6
34	13	1/92	12.198	0.32	46.0	**0.68**	**0.37**	0.01	0.18	2.5
34	13	2/94	12.198	0.32	46.0	**0.38**	**0.31**	0.002	0.03	0.32
34-m Operational Antennas										
34	24	5/94	11.922	0.33	46.3	**0.50**	**0.25**	0.007	0.1	1.27
34	25	6/96	11.913	0.33	47.0	**0.50**	**0.25**	0.007	0.1	1.27
34	26	10/96	11.913	0.33	47.0	**0.42**	**0.25**	0.004	0.05	0.76
34	54	5/98	12.502	0.32	43.2	**0.79**	**0.32**	0.02	0.25	4.0
34	34	6/98	12.748	0.315	48.3	**0.47**	**0.26**	0.006	0.08	1.2
34	55	7/03	11.450	0.33	43.1	**0.90**	**0.25**	0.03	0.41	5.8

* DSS = Deep Space Station (antenna's designation in the DSN):
DSS-14, 43, and 63 are the 70-m antennas
DSS-13 is the 34-m research and development (R&D) BWG antenna
DSS-24, 25, 26, 34, 54, and 55 are the 34-m BWG antennas

The accuracy in the final holographic maps and the resolution in of the images are interrelated. We formulated the accuracy from the simulation results to be

$$\sigma \cong 0.082 \frac{\lambda D}{\delta \mathrm{SNR}} \tag{8.2-1}$$

where

σ = standard deviation (accuracy) in recovering the mean position of a resolution cell

λ = wavelength

D = reflector diameter

δ = spatial resolution in the aperture plane (defined below)

SNR = beam peak voltage signal-to-noise ratio (SNR) in the test (antenna) channel.

Equation (8.2-1) agrees well with the analytical expressions derived in [2]. Here, the constant 0.082 was empirically determined based on the simulation results, which agree well with the analytically derived constant of $1/4\pi$. As will be shown in the simulation results, the accuracy across holographic maps varies with the aperture amplitude taper illumination. Results are better at the center of the dish and gradually become worse toward the edge of the dish. For a uniformly illuminated dish, accuracy stays relatively constant through most of the dish and quickly becomes worse just at the edge where the illumination falls off rapidly.

To define the angular resolution δ in the processed holographic maps, consider a square grid containing N^2 sampled data points separated by less than λ / D or one antenna beamwidth. Let

$$\Delta u = \Delta v = \frac{\mathrm{k}\,\lambda}{D} \tag{8.2-2}$$

where

$\Delta u, \Delta v$ = separation between two adjacent points in two orthogonal axes

k = a constant $0.5 < k < 1.0$

The length of this grid (L) is then:

$$L = N\,\mathrm{k}\left(\frac{\lambda}{D}\right) \tag{8.2-3}$$

Consider the Fourier transform of a rectangular pulse extended from $+(N/2)(\mathrm{k}\,\lambda D)$ to $-(N/2)(\mathrm{k}\,\lambda D)$. The function transforms from a pulse to:

$$\frac{\sin\left(\dfrac{\pi N\,\mathrm{k}\,\lambda x}{D}\right)}{\dfrac{\pi N\,\mathrm{k}\,\lambda x}{D}} \tag{8.2-4}$$

The two nulls of this function occur at $+D/\mathrm{k}\,\lambda N$ for a full null width of $2D/\mathrm{k}\,\lambda N$. We now define the spatial resolution to be at the 50-percent width and obtain:

$$\delta = \frac{D}{\mathrm{k}\,N} \tag{8.2-5}$$

where

δ = spatial resolution in the aperture plane

Aperture simulation models are used because of their simplicity and usefulness. They allow an examination of the interrelations between the standard deviation in the holographic maps and a known feature on the reflector surface. In these models, aperture and phase distribution are typically defined, and then far-field data are constructed. In general, an integration or FFT scheme may be used to obtain the far-field data. However, for certain special aperture distributions, such as those that are circularly symmetric, *closed-form* expressions can be used [13]. This allows an accurate and efficient far-field pattern generation. The steps of this aperture model follow.

The geometry of a circular aperture, with different annular regions designated by red and blue colors, is shown in Fig. 8-3. The green color represents a perfect dish surface relative to the best-fit paraboloid, while it is assumed that the red and blue colors represent regions that are deformed by a constant value of ±0.2 mm, respectively, causing constant phase irregularities and resulting in a main reflector surface error of 0.11-mm root-mean-square (rms). (Please note that the scale in Fig. 8-3 is ±0.35 mm). We further assume that the amplitude and phase distributions across the aperture are circularly

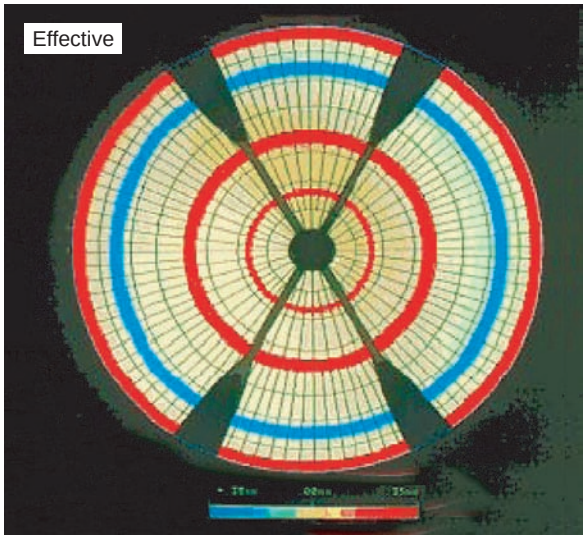

Fig. 8-3. Simulation I: geometry of simulated reflector distortions; no noise was injected.

symmetric, closed-form functions. These assumptions allow us to express the far-field integral in terms of a one-dimensional integral.

Furthermore, for an appropriately chosen amplitude distribution, this integral can be integrated in a closed form. This closed-form expression can be used to construct the far field pattern.

Once the far-field amplitude and phase data are generated, they can then be used in the error simulation algorithm by appropriately injecting noise in a manner that simulates the exact architecture of the holographic measurement system and its front-end thermal noise [9].

A narrow-bandwidth system can be designed with a wide dynamic range and linear response. Such a system will make use of geostationary satellite beacon signals (nearly CW) available on nearly all satellites at Ku-band (10.8 to 12.9 GHz), X-band (7.7 GHz), S-band (2.2 GHz), and on other bands as well. The antenna microwave holography receiver block diagram is shown in Fig. 8-4.

The back-end receiver uses synchronous detectors for the in-phase (I) and quadrature-phase (Q) components of the test and reference channels. The analog signal is digitized utilizing a 19-bit resolution analog-to-digital (A/D) converter, to form the ratio (rather than multiplication) of the test-to-reference channel signals. This provides the real and imaginary components of the complex far-field function. Amplitude variations in the satellite signal cancel out in the division operation. This feature is especially critical since no control over the satellite signal power level is available. Also, since the reference channel SNR in this scheme can easily be 40 dB or better, it can be safely used in the denominator. (This would not be desirable for weak reference signals.)

The antenna microwave holography provides a linear dynamic range of better than 96 dB down to integration periods of 0.2 millisecond (ms). When the satellite beacon effective isotropic radiated power (EIRP) is about 11 dB referenced to watts (dBW), a beam peak SNR of 73 dB is achieved on the 70-m antenna at Ku-band (12 GHz) with a 0.1-s integration period using a simple room-temperature field effect transistor (FET) (100 K) amplifier, while a 2.8-m reference dish provides 40–45 dB in SNR, using a room-temperature (100 K) FET.

For a multiplier integrator as well as a divider integrator receiver architecture, the effective signal SNR can be expressed as

$$\mathrm{SNR}_E = \left[\sqrt{\frac{1}{\mathrm{SNR}_T^2} + \frac{1}{\mathrm{SNR}_R^2} + \frac{1}{\mathrm{SNR}_T^2\,\mathrm{SNR}_R^2}} \right]^{-1} \tag{8.2-6}$$

where SNR_T and SNR_R are the test channel and reference channel SNR, respectively. The generality of this formulation makes it useful for many different receiver architectures.

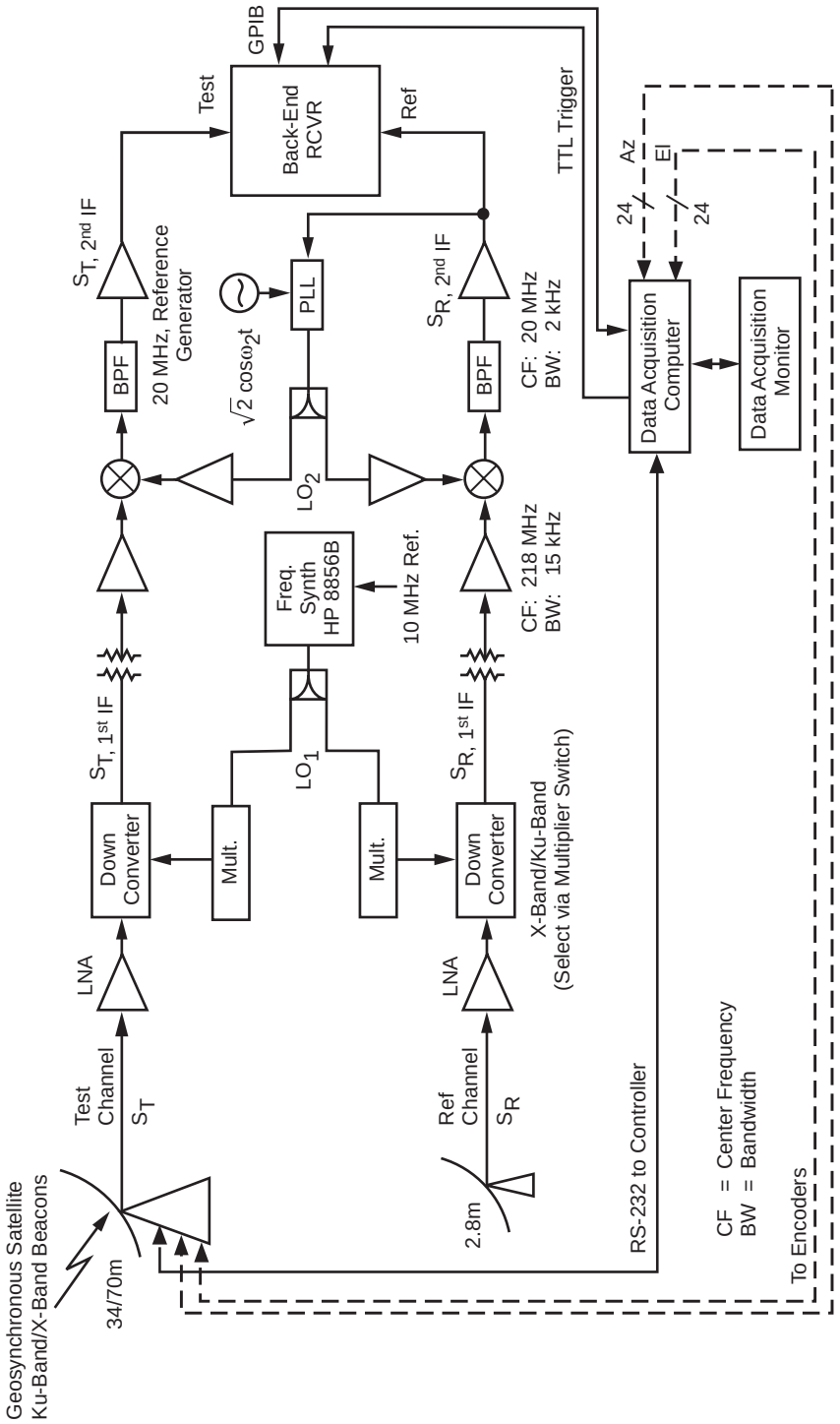

Fig. 8-4. Antenna microwave holography block diagram (notations defined in Section 8.3).

From Eq. (8.2-6), it is apparent that the effective SNR_E is dominated by the weaker of the two channels. What this means is that the beam peak SNR_T (of 73 dB) is not realized, and the first few data points on beam peak and a few sidelobes have an effective SNR_E (of approximately 45 dB) of the reference SNR_R. Once the test channel SNR_T drops below the reference antenna SNR_R (45 dB), it does degrade the effective SNR_E, which, from that point on, follows the same function as the test antenna beam patterns (SNR_T). This is acceptable since very few data points are affected (approximately 0.5 percent), and since by the nature of the data processing through the Fourier transform operation, all the data points in the far field contribute to each and every point in the aperture, as is shown in the simulations below.

A simulation algorithm was developed to derive the relationships between the standard deviation in the final holographic maps and the measurement SNR. The receiver back-end architecture, which comprises I and Q separation of both the test and reference channels, has been modeled in the simulation [9]. This was done by adding independent noise-processing components n, for which the 1σ in the random Gaussian function, for the test and reference signals, respectively, is

$$1\sigma_T = \frac{\mathrm{amp}_T(\max)}{\mathrm{SNR}_T} \tag{8.2-7}$$

where $\mathrm{amp}_T(\max)$ = beam peak amplitude in the test channel

$$1\sigma_R = \frac{\mathrm{amp}_R(\max)}{\mathrm{SNR}_R} \tag{8.2-8}$$

where $\mathrm{amp}_R(\max)$ = beam peak amplitude in the reference channel.

The function of the receiver described in Fig. 8-4 was used in the simulation to provide the resultant measured complex quantity, including noise:

$$\text{complex field} = \frac{\mathrm{amp}_T(\theta_i)e^{j\phi_{Ti}} + n_{R_i}^T + jn_{I_i}^T}{\mathrm{amp}_R\, e^{j0} + n_{R_i}^R + jn_{I_i}^R} \tag{8.2-9}$$

where

$\mathrm{amp}_T(\theta_i)$ = test antenna far-field amplitude voltage at the sampled data position θ_i.

ϕ_{T_i} = test antenna far-field phase at the sampled data position *i*.

$n_{R_i}^{T}$ = noise component in the complex real part of the digitized data sample *i* in the test channel.

$n_{I_i}^{T}$ = noise component in the complex imaginary part of the digitized data sample *i* in the test channel.

$n_{R_i}^{R}$ = noise component in the complex real part of the digitized data sample *i* in the reference channel.

$n_{I_i}^{R}$ = noise component in the complex imaginary part of the digitized data sample *i* in the reference channel.

$\text{amp}_R\, e^{j0}$ = reference channel far-field constant amplitude and phase value.

This simulation (Figs. 8-3, 8-5, 8-6, and 8-7) examined the effect of the SNR in the reference and test antennas on measurement accuracy.

In the simulation, four rings of panels were intentionally displaced by 0.2 mm ($\lambda/130$ at 11.45 GHz, Fig. 8-3). Three rings were displaced positively, and one was displaced negatively. The width of the three outmost rings was 2.0 m (76 λ), and the innermost rings was 1.0 m wide. The rms surface error of this model (Fig. 8-3) is 0.11 mm. The far-field for the above reflector geometry was generated and then contaminated with noise due to the front end, according to the model represented by Eq. (8.2-4). The far-field data were then processed to display the recovered surface error maps and to compute the surface rms errors.

In Fig. 8-3, Simulation I, the far-field was processed with no noise added to it. This simulated an SNR of more than 90 dB. The computer computational errors are at a level of about $\lambda/5000$ (11.45 GHz). By subtracting (map differencing) this model from subsequent simulations, we obtained a measure comparable to the measurement system standard deviation. Simulation II, (Fig. 8-5) models the conditions where the test antenna SNR on beam peak during the 0.1-s integration period is 73 dB, and the reference antenna constant SNR is 40 dB. The recovered rms of the test antenna surface is 0.12 mm, and the measurement system standard deviation is 0.07 mm ($\lambda/370$ at 11.45 GHz).

Simulation III, (Fig. 8-6) simulates conditions in which the test antenna beam peak SNR in the 0.1-s integration period is 68 dB and the reference antenna SNR is 40 dB. The recovered surface rms is 0.16 mm with a standard deviation of 0.13 mm.

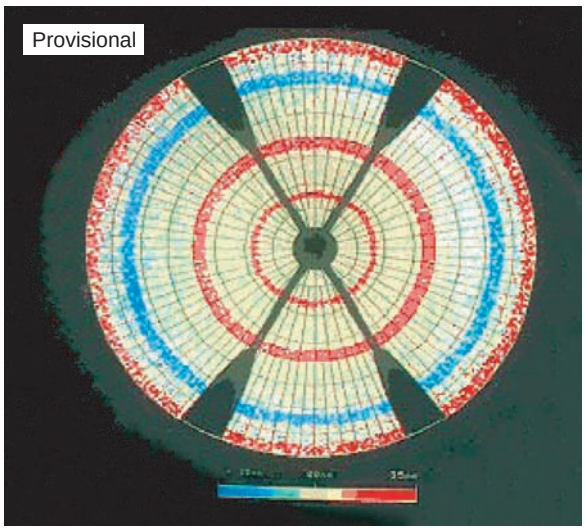

Fig. 8-5. Simulation II: test antenna SNR on beam peak in the 0.1-s integration period is 73 dB, and the reference antenna constant SNR is 40 dB.

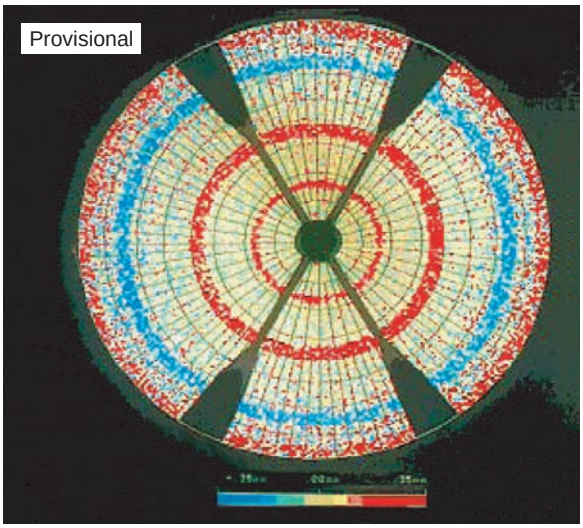

Fig. 8-6. Simulation III: test antenna beam peak SNR in the 0.1-s integration period is 68 dB, and the reference antenna constant SNR is 40 dB.

From simulation IV (Fig. 8-7), it is clear that the recovery of the dish surface error is very poor when the SNR drops to 58 dB. The recovered surface

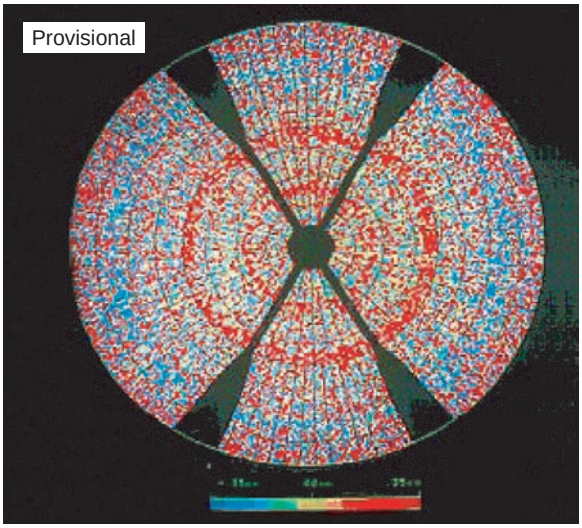

Fig. 8-7. Simulation IV: SNR dropped to 58 dB.

rms is 0.43 mm, and the standard deviation of this map is 0.41 mm. The necessity of a high-beam peak SNR for high-resolution, high-precision holographic measurement is clearly demonstrated [9].

8.3 Holography Receiver Signal Analysis

The MAHST design features a dual channel coherent CW receiver where the reference signal is provided by a small (2.8-m diameter dish) reference antenna, which is bore-sighted at a geostationary satellite while the antenna under test (AUT) is acquiring the signal while performing a continuous raster-scan relative to the moving spacecraft (see Figs. 7-4 and 8-1).

Referring to Fig. 8-4, the microwave signal at the test antenna (upper channel) may be modeled as

$$S_T = \sqrt{2P_T(t)}\sin(\omega_o t + \theta + \varphi) \tag{8.3-1}$$

where

S_T = test signal

$P_T(t)$ = nominal power of the received signal at the test channel

ω_o = nominal (angular) frequency ($2\pi f_o$) of the received microwave test signal

θ = the function account for Doppler effect

φ = phase

The departure of the instantaneous frequency from its nominal value of ω_o is accounted for by the time derivative of θ. The purpose of the receiver is the measurement of the test antenna amplitude and phase represented by square root of $2P_T(t)$ and φ.

The microwave signal at the reference antenna is modeled as

$$S_R = \sqrt{2P_R(t)}\sin(\omega_o t + \theta) \tag{8.3-2}$$

where:

S_R = reference signal

$P_R(t)$ = nominal power of the received signal in the reference channel

The reference channel serves as a phase reference for the phase measurements, as well as for tracking out the Doppler effects introduced by the movement's drifts of the spacecraft. The one-sided noise spectral density N_{OT} of the receiving channels equals the equivalent noise temperature multiplied by Boltzmann's constant. The equivalent noise temperature in the two channels must be referenced to the same point in the receiving chain (for example, the input of the low-noise amplifier).

The frequency of the local oscillator (LO) in the first down-converter mixer in the receiver front end is selectable via three multipliers to cover the entire Ku-band frequency range of 10.8 to 12.8 GHz, as well as X-Band (7.7 GHz). The first LO (LO_1) is common to both the test and the reference channels for phase coherent detection, and it can be modeled as

$$\mathrm{LO}_1 = 2\cos\left[\left(\omega_o - \omega_1\right)t\right] \tag{8.3-3}$$

where ω_1 is the nominal (angular) frequency of the signal in the first intermediate-frequency (IF) stage. The resultant signals output of the first down conversion stages become:

$$S_{T,1\mathrm{IF}} = \sqrt{2P_T(t)G_T}\,\sin\left(\omega_1 t + \theta + \varphi + \xi\right) \tag{8.3-4}$$

and

$$S_{R,1\mathrm{IF}} = \sqrt{2P_R(t)G_R}\,\sin\left(\omega_1 t + \theta\right) \tag{8.3-5}$$

where ξ is the differential phase delay between the reference and test channels. G_T and G_R are the power gains in the test and reference channels,

respectively. The one-sided noise spectral densities within the first IFs are $N_{OT}G_T$ and $N_{OR}G_R$.

The second LO (LO_2) is derived from the output of a phase-locked loop (PLL) that tracks the reference channel signal Doppler effects. The PLL itself is tied into the Frequency and Timing Subsystem (FTS) station standard stable oscillator.

$$\mathrm{LO}_2 = 2\cos\left[\left(\omega_1 - \omega_2\right)t + \theta - \phi\right] \tag{8.3-6}$$

The PLL output is used to further down convert the first IF signals in the test and reference channels. When the PLL tracks perfectly, $\phi = 0$. The test and reference signals in the second IF stages are then given by:

$$S_{T,\,2\,\mathrm{IF}} = \sqrt{2P_T(t)G_T}\,\sin\left(\omega_2 t + \varphi + \xi + \phi\right) \tag{8.3-7}$$

and

$$S_{R,\,2\,\mathrm{IF}} = \sqrt{2P_R(t)G_R}\,\sin\left(\omega_2 t + \phi\right) \tag{8.3-8}$$

where ω_2 is the nominal (angular) frequency of the second IF and ϕ is the phase-tracking error in the PLL.

The gains of the channels between the first and second IFs are incorporated into G_T and G_R. The differential phase delay between the reference and test channels that occurs between the first and second IFs is incorporated into ξ. The one-sided noise spectral densities within the second IFs are $N_{OT}G_T$ and $N_{OR}G_R$.

The phase transfer function of the PLL is given by:

$$H(s) = \frac{KF(s)}{s + KF(s)} \tag{8.3-9}$$

where

$H(s)$ = Laplace transform
K = cumulative loop gain
$F(s)$ = transfer function of the loop filter

The noise-equivalent bandwidth B of this phase transfer functions is:

$$B = \int_0^\infty |H(j2\pi f)|^2\, df \tag{8.3-10}$$

and the loop phase error variance is:

$$\sigma_\phi^2 = \frac{N_{OR}B}{P_R} \tag{8.3-11}$$

The back-end portion of the receiver measures the amplitude and phase of the signals in the test channel second IF relative to the amplitude and phase of the signal in the reference channel second IF. It is this relative amplitude and phase that is required for holography measurements.

The test channel signal is given by Eq. (8.3-7) and that of the reference channel by Eq. (8.3-8). The frequency of these two signals is stable because the PLL has removed the time-varying Doppler effect. It might seem that the gains G_T and G_R and the differential phase delay ξ obscure the parameters of interest. For the purpose of holography, however, it is only necessary to measure how the relative amplitude and phase change with time. As long as G_T, G_R, and ξ remain approximately constant during the course of the observation. The receiver back-end works as follows. The test and reference channel signals (at approximately 20 MHz) are further downconverted to 100 kHz. The signals are then subjected to automatic gain control (AGC). In each channel, there are in-phase and quadrature detectors followed by analog-to-digital (A/D) converters. The amplitude and phase of the test signal relative to the reference signal are computed as described by Eq. (8.2-9). The AGC removes much of the amplitude variation from the signals. This is not a problem because the variations applied to each channel are recorded. Recorded AGC gain represents a coarse measure of the signal amplitude. These recorded AGC values are then entered into the final calculation of the relative amplitude.

The relative phase $\varphi + \xi$ is measured. As mentioned above, as long as the instrumental delay ξ is approximately constant during the observation; the variation of φ is reflected in the measured result. The loop phase error ϕ is not present because it is a common-mode error in the test and reference signals. (However, it is still important to keep the loop phase error variance Eq. (8.3-11) small in order to minimize cycle slips in the loop.) The variance in the relative phase measurement due to receiver noise is given by

$$\frac{N_{OT}}{2P_T\,\mathrm{T}} + \frac{N_{OR}}{2P_R\,\mathrm{T}}\ \mathrm{rad}^2 \tag{8.3-12}$$

where T is the integration time for each measured phase.

By the virtue of the reference antenna continuous boresight on the spacecraft signal source, under ideal conditions its signal power would be a constant during the observation period. In addition, if the gains of the test and

reference channels would also stay constant during the measurements, under these conditions the relative amplitude measured would be:

$$\sqrt{\frac{P_T(t)G_T}{P_R G_R}} \tag{8.3-13}$$

This is proportional to the test antenna far-field pattern amplitude.

The variance in the relative amplitude measurement due to receiver noise is given by

$$\frac{P_T G_T}{P_R G_R}\left[\frac{N_{OT}}{2P_T\,\mathrm{T}} + \frac{N_{OR}}{2P_R\,\mathrm{T}}\right] \tag{8.3-14}$$

where T is the integration time for each measured amplitude.

In practice, the antenna microwave holography receiver was designed with a second-order PLL exhibiting a lag-lead loop filter and a selectable (variable) phase-locked loop (PLL) bandwidth designed to operate with phase noise values of 1–3 deg at 50 dB-Hz. This enables the receiver to track over a wide range of the commercially available geosynchronous satellites.

Figure 8-8 shows typical antenna far-field amplitude and phase pattern measured by the antenna microwave holography receiver described above. Figure 8-8 is the result of sampling a 127 × 127 data array from a 34-m diameter antenna (DSS-13) scanning at ±2.65 deg relative to the satellite nominal position.

8.4 Mathematical Formulation Data Processing

The mathematical relationship between an antenna far-field radiation pattern (T) and the antenna surface-induced current distribution (J) is given by

$$\begin{aligned}\vec{T}(u,v) = \iint_S \tilde{J}(x',y')\exp(jkz')\bullet\left[\exp\left[-jkz'(1-\cos\theta\right]\right] \\ \bullet\exp\left[jk(ux'+vy')\right]dx'dy'\end{aligned} \tag{8.4-1}$$

where

$z'(x',y')$ = defines the surface S

u, v = direction cosine space

θ = observation angle

For a small angular extent of the far-field pattern, this expression reduces to

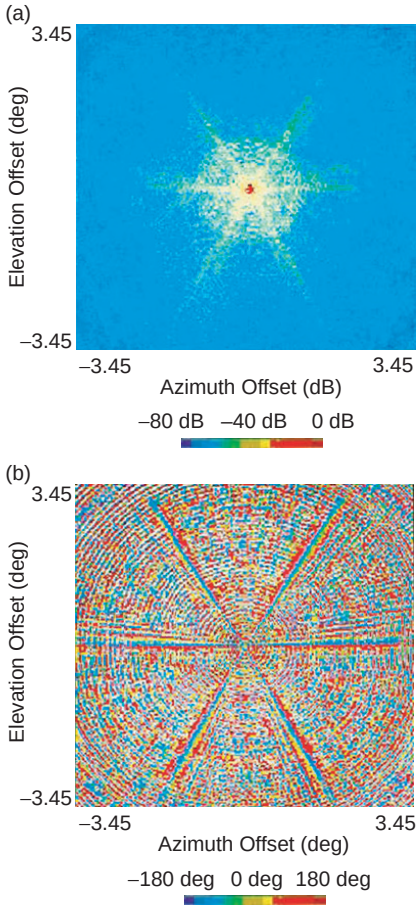

Fig. 8-8. Antenna far-field pattern measured by antenna microwave holography at Ku-band (12-GHz) showing (a) amplitude and (b) phase.

$$\vec{T}(u,v) = \iint_s \tilde{J}(x',y')\exp(jkz')\bullet\exp\left[jk(ux'+vy')\right]dx'dy' \qquad (8.4\text{-}2)$$

Equation (8.4-2) is an exact Fourier transform of the induced surface current. To derive the residual surface error, geometrical optics ray tracing is used to relate the normal error, ε, to the axial error and phase in a main-reflector paraboloid geometry (Fig. 8-9):

$$\frac{1}{2}\Delta PL = \frac{1}{2}\left[P^1P + PQ\right] = \frac{1}{2}\left[\frac{\varepsilon}{\cos\varphi} + \frac{\varepsilon\cos 2\varphi}{\cos\varphi}\right] = \varepsilon\cos\varphi \qquad (8.4\text{-}3)$$

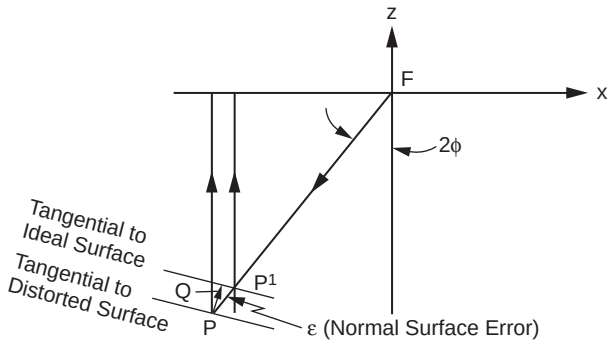

Fig. 8-9. Surface distortion geometry.

$$\text{Phase}\,(\Delta PL) = \frac{4\pi}{\lambda}\varepsilon\cos\varphi \tag{8.4-4}$$

and

$$\cos\varphi = \frac{1}{\sqrt{1+\dfrac{X^2+Y^2}{4F^2}}} \tag{8.4-5}$$

where F is focal length.

Allowing for the removal of a constant phase term and substituting Eq. (8.4-4) into Eq. (8.4-2) yields

$$\begin{aligned}\vec{T}(u,v) = \exp(-j2kF)\iint_s \tilde{J}(x',y')\bullet\exp\left(j4\pi\frac{\varepsilon}{\lambda}\cos\varphi\right)\\ \bullet\exp\left[jk(ux'+vy')\right]dx'dy'\end{aligned} \tag{8.4-6}$$

For the processing of sampled data, the associated discrete Fourier transform (DFT) is utilized:

$$\begin{aligned}T(p\Delta u, q\Delta v) = sx\ sy\sum_{n=-N1/2}^{N1/2-1}\sum_{m=-N2/2}^{N2/2-1} J(nsx, msy)\\ \bullet\exp\left[j2\pi\left(\frac{np}{N1}+\frac{mq}{N2}\right)\right]\end{aligned} \tag{8.4-7}$$

where

$N1\times N2$ = measured data array size

sx, sy = sampling intervals on the aperture, coordinates

n, m, p, q = integers indexing the discrete samples

$\Delta u, \Delta v$ = sampling interval in the far-field space

Since the magnitude of the far-field pattern is essentially bounded, the fast Fourier transform (FFT) is usually used for computation, and it is symbolized here by (F). Solving for the residual normal surface error and substituting Eq. (8.4-5), we obtain

$$\varepsilon(x,y) = \frac{\lambda}{4\pi}\sqrt{1+\frac{x^2+y^2}{4F^2}}\,\text{Phase}\left[\exp(j2kF)F^{-1}\left[T(u,v)\right]\right] \qquad (8.4\text{-}8)$$

The spatial resolution in the final holographic maps was defined in Eq. (8.2-5).

The resulting aperture function needs to be corrected for modulo-2π phase errors and a global least-squares fit performed on the data to the "best-fit" paraboloid. This process also allows for the correction of antenna-pointing errors introduced during the measurement. The "best-fit" paraboloid is found by minimizing S, the sum squares of the residual path length changes:

$$S = \sum_{i=1}^{N^2} \Gamma(\Delta PL_i)^2 A_i \qquad (8.4\text{-}9)$$

where

Γ = support domain constraints masking operator

ΔPL_i = path length change

A_i = amplitude weighting factor

with respect to 6 degrees-of-freedom of the reflector motion; three vertex translations, two rotations, and a focal length change. The six partial differential equations, which are solved simultaneously, are of the form [14]:

$$\frac{\partial S}{\partial \text{Par}} = 2\sum_{i=1}^{N^2} \Gamma \frac{\partial \Delta PL_i}{\partial \text{Par}} \Delta PL_i A_i = 0 \qquad (8.4\text{-}10)$$

where Par is one parameter of the 6 degrees-of-freedom.

It is correct to apply the best-fit paraboloid algorithm to either the conventional Cassegrain paraboloid-hyperboloid or dual-shaped reflector systems even though the latter do not use a paraboloid as the main reflector. Either design is a planewave-to-point source transformer, differing only in the field intensity distribution. The resultant aperture function at the end of this process is referred to as an "Effective Map" since it includes all phase effects that are contributing to the antenna performance. These effects include the subreflector scattered (frequency-dependent) feed phase function. Removal of the feed-phase function and subreflector support structure diffraction effects

results in a frequency independent map, which is referred to below as the "Mechanical Map."

Panel setting information is derived by sorting together all the data points within each panel and performing a least-squares fit. The algorithms allow for one translation and two rotations, S^k, α^κ, β^κ; hence, it can be referred to as a rigid body motion. For each panel and its associated *n* data points, we solve for the motion parameters via Eq. (8.4-11) (Fig. 8-10). This mathematical process also increases the accuracy in determining the screw adjustment correction [14] by a factor of $\sqrt{n}$.

$$\begin{bmatrix} \sum_{i=1}^{n}\cos^2(\gamma_i) & \sum_{i=1}^{n} d_i * \cos^2(\gamma_i) & -\sum_{i=1}^{n} e_i * \cos(\gamma_i) \\ \sum_{i=1}^{n} d_i * \cos^2(\gamma_i) & \sum_{i=1}^{n} d_i^2 * \cos^2(\gamma_i) & -\sum_{i=1}^{n} e_i * d_i * \cos(\gamma_i) \\ -\sum_{i=1}^{n} e_i * \cos(\gamma_i) & -\sum_{i=1}^{n} d_i * e_i * \cos(\gamma_i) & \sum_{i=1}^{n} e_i^2 \end{bmatrix} \begin{bmatrix} S^k \\ \alpha^\kappa \\ \beta^\kappa \end{bmatrix} = \begin{bmatrix} -\sum_{i=1}^{n} \varepsilon_i * \cos(\gamma_i) \\ \sum_{i=1}^{n} \varepsilon_i * d_i * \cos^2(\gamma_i) \\ \sum_{i=1}^{n} \varepsilon_i * e_i * \cos(\gamma_i) \end{bmatrix} \quad (8.4\text{-}11)$$

For optimal telecommunication performance in terms of *G*/*T*, the Cassegrain dual shaped-reflector antenna system has the advantage of providing higher aperture gain and aperture efficiency relative to the traditional paraboloid–hyperboloid Cassegrain design. However, for radio astronomy, where high beam efficiency is needed, the latter provides the better choice. The

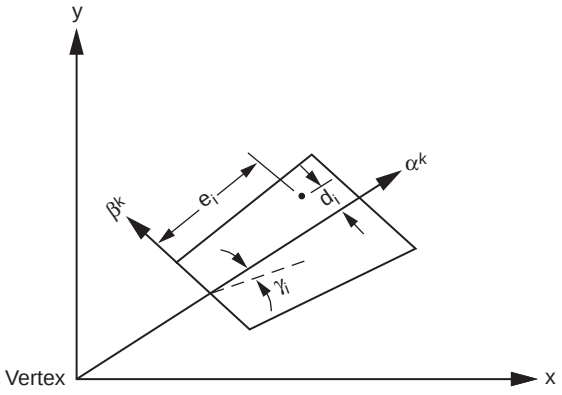

Fig. 8-10. Reflector panel geometry.

challenge of holographic applications for these antenna systems is the high level of diffraction effects, due to the subreflector edge, appearing towards the edge of the dish main reflector aperture (see simulation of feed diffraction effects on holographic processing Fig. [8-11(a)]). The holographic map that includes these effects is termed “Effective Map” in contrast to the “Mechanical Map” where the diffraction effects have been removed. If the diffraction effect due to the feed phase function is kept during the derivation of the panel setting corrections, it will tend to mechanically “tune” and improve the dish performance at the measurement frequencies, but it will degrade the dish performance at other frequencies. If the antenna performance is to be optimized over a wide range of operating frequencies, as is the casee for the NASA-JPL-antennas, the diffraction effects must be removed prior to deriving the panel setting correction. Figure 8-11(b) shows the “Mechanical Map” where diffraction effects were reduced considerably resulted from applying the diffraction cancellation operation [14]. The error in panel setting correction resulted from the residual diffraction effect is on the order of 30 micrometers (μm).

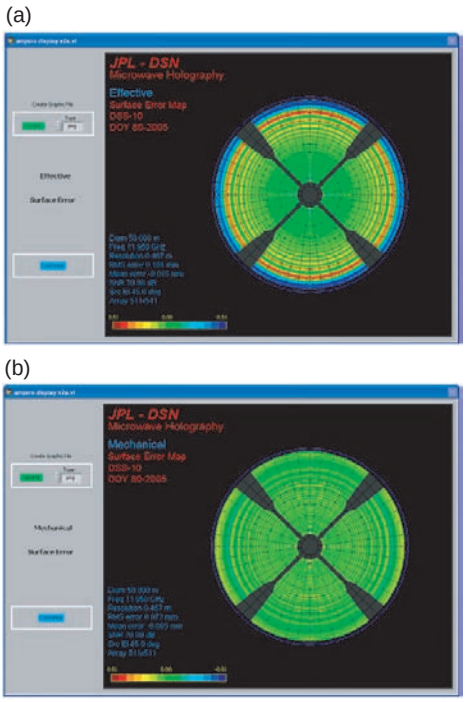

Fig. 8-11. Simulated maps, including (a) simulated effective map and (b) simulated mechanical map.

8.5 Applications

8.5.1 34-m BWG Research and Development Antenna

In August 1990, holographic measurements from the Cassegrain *f*1 focus of the new DSS-13 BWG antenna in Goldstone, California, were made (Fig. 8-12 and Fig. 7-2). Strong CW signals from geostationary satellite beacons were used as far-field sources. Three different geostationary satellites were scanned, producing high- and medium-resolution data sets at elevation angles of 46.5, 37, and 12.7 deg The measurements obtained provided the necessary subreflector position information, panel setting information, a look at the adjusted surface of the antenna, and information about the gravity performance of the structure at a low elevation angles. The holographic antenna measurements used satellite signal and ephemeris information supplied by several commercial companies for GTE (GSTAR W103), GE (SatCom K1), and ComSat (Intelsat V).

Functionally, the outer 0.6 m of the DSS-13 antenna is designed as a noise shield. The rms error obtained from analysis of the central 32 m of the antenna is, therefore, more representative of the actual surface than the rms obtained from examination of the full 34-m dish. Therefore, we will present here only the rms values for the central 32 m of the antenna. The precision in the derived surface error maps is 0.05 mm (50 μm). In general, the indicated rms increases as the lateral resolution of the measurement increases (i.e., δ is a smaller numerical value) (Eq. (8.2-1). This is an expected result as there is less area averaging occurring as the resolution increases. The asymptotic or infinite

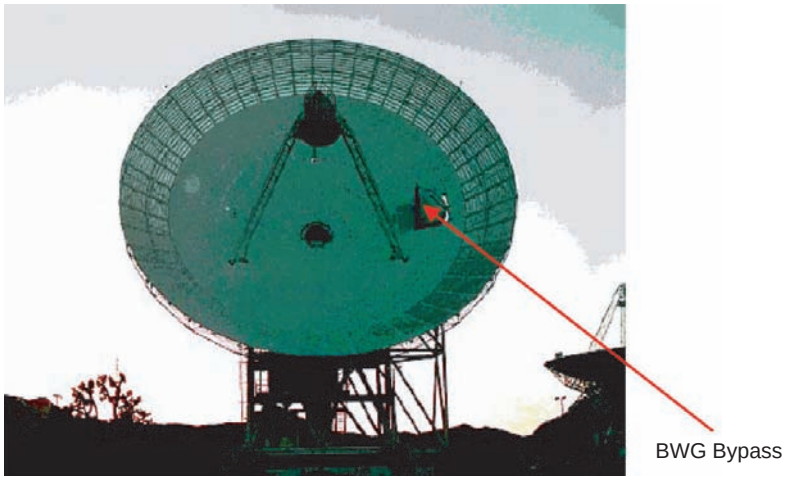

Fig. 8-12. The DSS-13 BWG antenna, which includes the BWG bypass structure in August 1990.

resolution rms can be estimated by analyzing the scan data at varying resolutions.

It is estimated that the rms error found by holography high-resolution (0.32-m) scans is 8 percent below the infinite resolution rms. Figure 8-13 shows the surface error map of the central 32 m of the DSS-13 antenna surface as found on August 28, 1990, at 46.5 deg elevation. The main reflector surface normal rms error was found to be 0.88 mm (0.77 mm axial) at a resolution of 0.32 m [15,16].

This measurement supplied the data required for verifying the subreflector position, analyzing the antenna surface, and providing the panel-setting information. The surface images derived from the aperture-plane phase represent the antenna surface deviations from ideal in the surface normal direction. In the images, the subreflector, the tripod and its shadows, and the bypass beam waveguide are intentionally masked out. The remaining surface is overlaid with an outline of each reflecting panel. The surface error information is shown in pseudo color, with red and blue indicating the high and low deviations of ±1.25 mm, respectively. The panel-setting information derived from this scan was applied to the 348 panels adjusted by the 1716 adjustment screws for this antenna. As a scheduling expedient, it was decided to adjust the surface panels by turning the adjusting screws to the nearest 1/8 of a turn (0.16 mm). Screws requiring adjustment of less than ±1/8 of a turn were not touched.

Figure 8-14 was derived on September 7, 1990 after the first application of holography panel resetting. The image reveals that the panels in the outer two rings are overbent. The rms surface error achieved by holography-based rigid

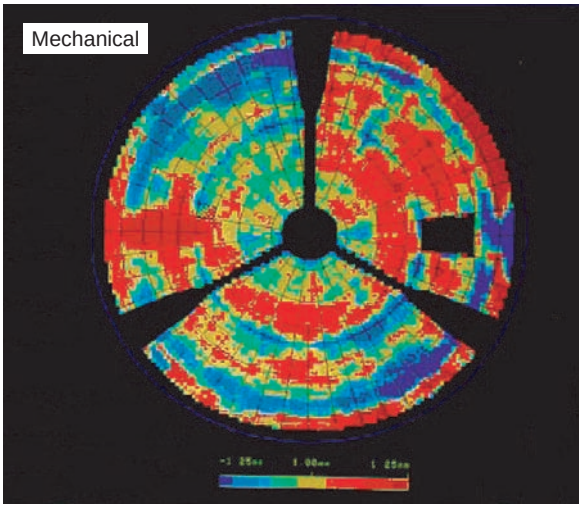

Fig. 8-13. DSS-13 after the initial theodolite setting.

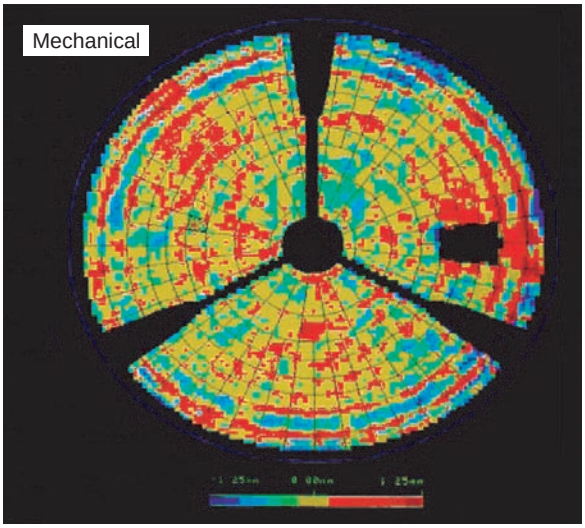

Fig. 8-14. DSS-13 after first application of holography.

body panel adjustment is 0.43 mm surface normal at a resolution of 0.32 m (Table 8-1). The post-holography surface provides a performance improvement (G/T) of about 0.32 dB at X-band (8.45 GHz), and 4.6 dB at Ka-band (32 GHz). The measured antenna efficiency at 46 deg elevation, after the holography panel setting, was 52.3 percent at Ka-band (32 GHz) and 75.4 percent at X-band (8.45 GHz) [15,16].

Please note that additional gain improvements due to subreflector position corrections are not accounted for in Table 8-1.

8.5.2 Gravity Performance of the BWG Antennas

The surface-error map shown in Fig. 8-15 was derived from medium-resolution, 0.80-m holography measurements made on September 18, 1990 at an elevation angle of 12.7 deg. The surface normal rms error at this low elevation angle and resolution is 0.50 mm. The measured antenna efficiency at 12.7 deg elevation was 39.4 percent at Ka-band and 74.0 percent at X-band.

The asymmetry revealed in this holographic low elevation map is attributed to the beam waveguide (BWG) bypass structure (shown in Fig. 8-12). Expectations were that removing the bypass would eliminate the asymmetrical gravity distortion and improve the 32-GHz gravity performance of the antenna. After the removal of the bypass BWG, and replacement with four panels, the measured gravity distortion function was indeed symmetrical (Fig. 8-16). However, the performance of the antenna as a function of elevation angle did not improve. Actually, the antenna gravity performance roll-off after the bypass

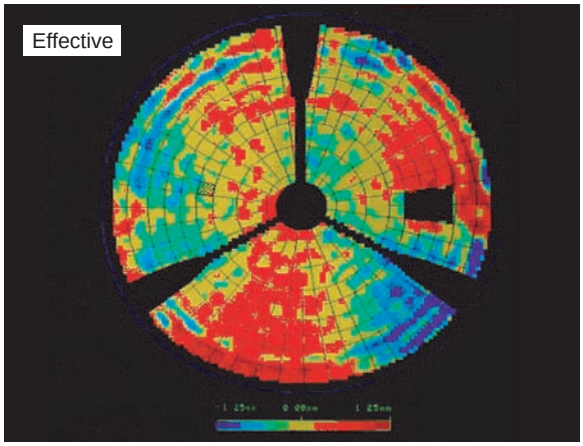

Fig. 8-15. Holographic surface-error map imaging at 12.7-deg elevation.

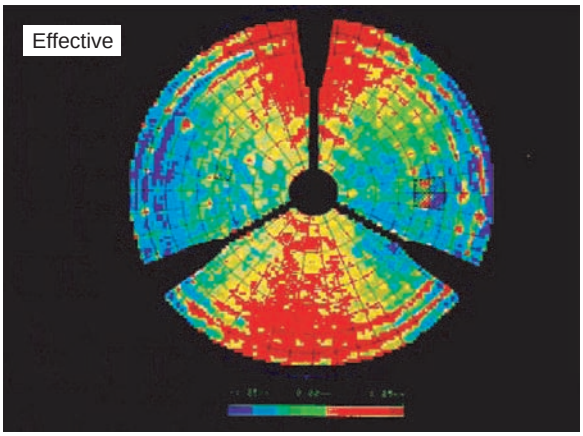

Fig. 8-16. DSS-13 imaging at 12.5-deg elevation after removing the bypass.

removal was 2.3 dB between 46- and 12.7-deg elevations at Ka-band, while with the bypass in place, it was only 1.2 dB. From this test (and combined with structural analysis by Roy Levy [17]) it was clear that the bypass structure, although causing asymmetrical gravity response, was adding significant stiffness to the antenna backup structure—a highly desirable feature for improved Ka-band performance. This lesson was applied to all future NASA–

JPL DSN 34-m BWG antennas, building them stiffer, and thereby achieving a gravity deformation loss of only 1.0 dB at Ka-band. (The new 34-m BWG antennas have a quadripod support for the subreflector instead of a tripod and this increases stiffness significantly.

Figure 8-17 shows the mechanical surface error map that was obtained (January 1992, Table 8-1) from the holographic measurements made on the DSS-13 after the removal of the BWG bypass and the application of a second holographic panel setting to the antenna. The normal rms surface error achieved was 0.38 mm, which agrees well with the 1990 predicted (best achievable by panel setting) surface of 0.36 mm. This reduction in rms (down from 0.43 mm) contributed an additional 0.26-dB performance increase (G/T) at Ka-band. The deformed panels in rings 8 and 9 are clearly noticeable in Fig. 8-17. The images in Fig. 8-17 were derived at Ku-Band (12.1795 GHz) by raster-scanning the antenna beam across a commercial geostationary satellite. The very high lateral

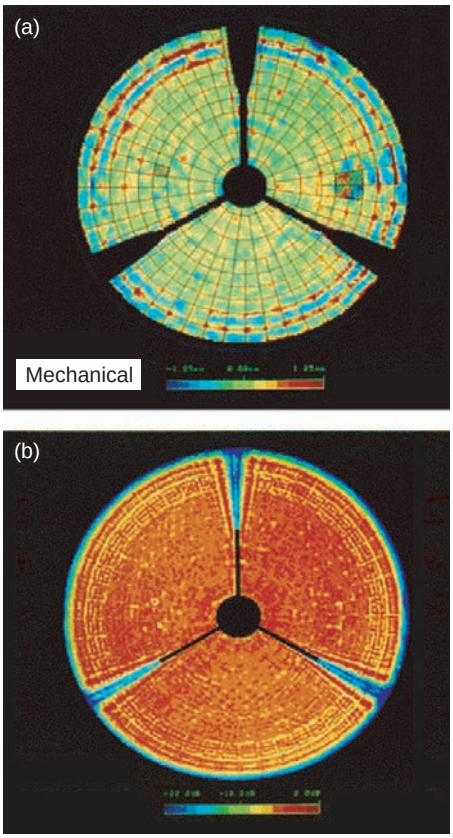

Fig. 8-17. Super-high resolution, 20-cm holographic imaging of DSS-13 showing (a) surface error and (b) current intensity map.

resolution of 20 cm is the result of a complex data array of 38,809 (197 × 197) samples of the far field of the antenna; the data array includes sampling to the antenna 150th sidelobe. The surface current intensity map (Fig. 8-17(a)) and surface error (Fig. 8-17(b)) confirm features of the antenna's mechanical and electromagnetic designs. These images also provide information that can be used to physically correct a broad range of possible design deficiencies. Irregularities in the shape of the reflecting surface and in the intensity (power) distribution are revealed in the "light" of the microwave illumination. The surface-current map confirms the uniform illumination design of this dual-shaped reflector antenna.

Each of the 348 individual reflecting panels, as outlined in the surface-error map, is characterized by an average of 94 accurate data cells, from which information to mechanically adjust each panel is derived and applied by adjusting the 1716 antenna adjustment screws.

The rms surface achieved of $\lambda/25$ is capable of operating at Ka-band with only 0.4-dB efficiency loss due to surface rms error. Estimates based on holographic measurements before and after adjustment of the surface indicate that more than 4 dB of performance was gained at 32 GHz. Radiometric measurements of antenna efficiency at 32 GHz confirm the excellent results obtained through the application of microwave holography.

During the planning stages of the DSS-13 BWG antenna project in 1988, it was decided to compromise and manufacture the main reflector panels by utilizing the existing DSS-15 34-m High Efficiency (HEF) antenna panel molds. The differences in the shape of the panels were thought to be minor, and it was believed that they would not significantly affect the required performance of the new research and development antenna. After the initial holographic imaging of DSS-13, it was clear from the images that the panels in rings 8 and 9 were systematically overbent (especially noticeable in the super-high resolution map of Fig. 8-17). Assuming that the panels on the DSS-13 antenna were made accurately from the DSS-15 manufacturing contours, the panels were mathematically best-fitted to the DSS-13 design contour. The axial errors between these two contours were calculated for each of the nine rings and then subtracted from the reference DSS-13 required shape.

The errors in the first seven panel rings are minor and cause no significant loss at 32 GHz. The errors in rings 8 and 9 are much more sizable (smooth curves in Figs. 8-18 and 8-19) and contribute noticeably to the antenna RF performance at 32 GHz. The step-wise linear plots in Figs. 8-18 and 8-19 are the holographically derived errors in the panels in rings 8 and 9. The holography data are sampled over seven points across each panel, and these data agree very well with the mechanically derived smooth curves. Indeed, when we compute the antenna rms error for the inner seven rings only in Fig. 8-17, the result is 0.28 mm, while the rms error for the outer rings 8 and 9 (excluding the noise shield) is 0.60 mm [16].

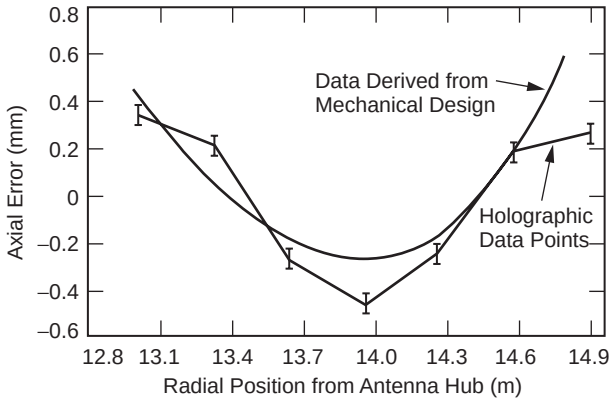

Fig. 8-18. Mechanical error in panel ring 8.

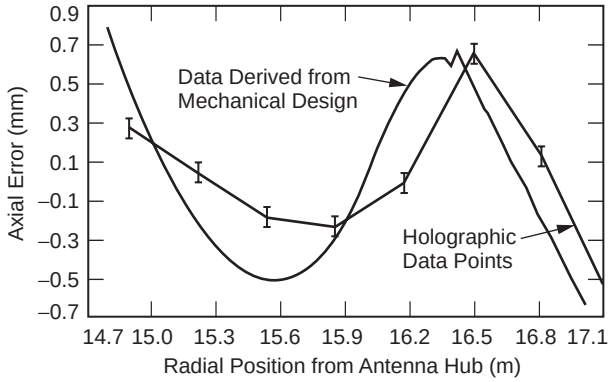

Fig. 8-19. Mechanical error in panel ring 9.

The potential increase of performance at Ka-band by achieving 0.28-mm rms for the entire dish is 0.6 dB. The DSS-13 antenna efficiency at the time of these measurements was 52 percent at f1 focus at Ka-Band (32 GHz), and it was predicted that the antenna efficiency would increase to 60 percent if the 0.6-dB opportunity were pursued. This proved to be the case; the current efficiency of the DSN 34-m BWG subnet antennas is 60 percent from f3 focus due to their effective rms of 0.25 mm, which was established by the microwave holography technique.

Replacing the damaged bent panels in rings 8 and 9 would have cost $300k; so instead a proposal to unbend them using the holographic technique was accepted. During the early part of February 1994, holographic measurements were made at DSS-13 to apply the panel unbending procedure to the panels in rings 8 and 9. The DSS-13 antenna surface error was further reduced from 0.38 mm to 0.31 mm corresponding to an additional 0.32 dB performance improvement at Ka-band (Table 8-1). Applying a total of four panel

setting/unbending sessions at DSS-13 between 1990 and 1994 resulted in reduction of its surface rms error from an initial 0.88 mm to 0.31 mm, which improved its RF performance at Ka-band (32 GHz) by approximately 5.3 dB. The efficiency of the DSS-13 measured from the BWG focus (F3) is 57 percent. This corresponds to an estimated efficiency from the Cassegrain F1 focus of approximately 65 percent.

8.5.3 Operational DSN 34-m BWG Antenna Network

Between May of 1994 and July of 2003, six newly constructed NASA–JPL DSN 34-m BWG antennas were measured holographically, and their panels and subreflectors were set and aligned. Three of the six antennas are located in the Goldstone Deep Space Communication Complex (GDSCC) in California and are designated DSS-24, DSS-25, and DSS-26. Two 34-m BWG antennas (designated DSS-54, and DSS-55) are located near Madrid, Spain (MDSCC), and one 34-m BWG antenna (designated DSS-34) is located near Canberra, Australia (CDSCC). The summary results of these measurements are presented in Table 8-1.

At GDSCC, the measurements were made from the Cassegrain F1 focus, utilizing a Ku-band (11.9-GHz) beacon signal from the GSTAR-4 satellite observed at the nominal elevation angle of 47 deg. Gravity and performance measurements at low elevation angles were taken using the beacon signal of the Intelsat-307 satellite observed at the nominal elevation angle of 12.7 deg. At 47-deg elevation, the normal rms surface errors of the DSS-24, DSS-25, and DSS-26 (as set by the theodolite) were 0.50 mm, 0.50 mm, and 0.42 mm, respectively (Table 8-1). Figure 8-20 shows the holographically derived surface error map of DSS-24 after the alignment of the panels using the theodolite technique, achieving a normal rms surface error of 0.50 mm [18,19].

Figure 8-21 shows the holographically derived surface error map of DSS-24 after applying only one session of holography derived panel setting, achieving a normal rms surface error of 0.25 mm (the color scales in the images of Figs. 8-20 and 8-21 is ±1.25 mm). The 34-m BWG network antennas have 348 panels and 1716 adjusting screws, with the rms surface of the individual panels specified at 0.127 mm, and the rms surface error of the subreflector is 0.125 mm. Since a precision panel adjusting tool was not used in order to reduce antenna down time, the panel listing data were rounded to the nearest ±1/8 of a screw turn. This enabled resetting the entire dish in an 8-hour period. The inferred root sum square (rss) panel setting accuracy is therefore 0.175 mm rms. The precision of the antenna surfaces in terms of diameter/rms is 1.36×10^5, and the gain limit of the antennas occurs at 95 GHz. The resulting measured efficiencies of the antenna from the Cassegrain f1 focus at 46.3-deg elevation were: 75.25 percent at X-band and 60.6 percent at Ka-band

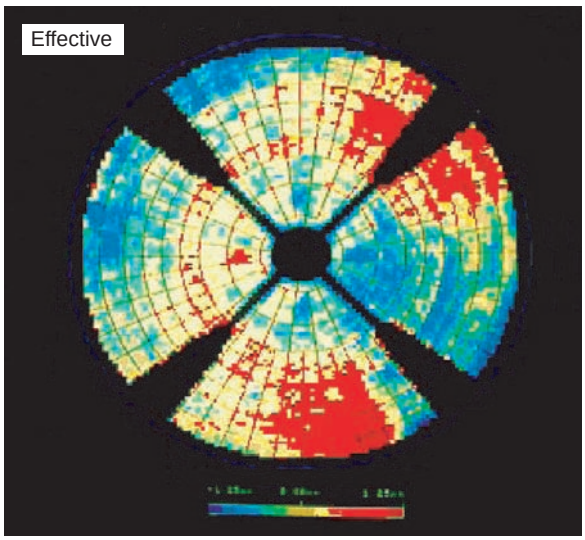

Fig. 8-20. Holographically derived DSS-24 surface error map before holographic alignment (theodolite alignment only), 0.50-mm rms.

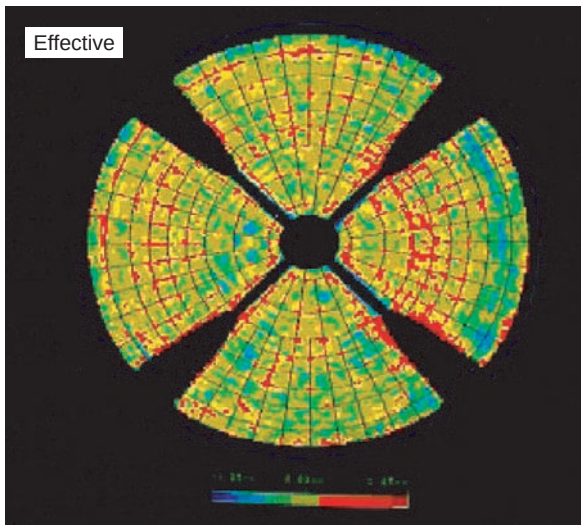

Fig. 8-21. DSS-24 surface-error map after holographic alignment, 0.25-mm rms.

(referenced to the input LNA). At 32 GHz (Ka-band), the averaged improved performance for each of the GDSCC antennas due to holography panel setting is estimated to be 1.1 dB. The antennas rms surface error at 12.6-deg elevation

averages approximately 0.50 mm, and it is mostly characterized by astigmatism due to gravity deformation, as expected.

The conventional process was used to set the panels of the first five 34-m BWG antennas (Table 8-1) that came on line. This process consisted of initial theodolite metrology panel setting to bring the antenna rms surface error down to 0.54 mm (0.02 in.), followed by holographic panel setting that further reduced the antennas rms error to 0.25 mm. The theodolite panel setting typically required 6 weeks of antenna down time. Given the experienced gain with these five antennas, and noticing the high efficiency of the holographic panel setting application, it was decided to relax the (total station) theodolite setting to a "rough" 1.0 mm (0.05 in.) (thereby reducing the antenna down time from 6 weeks to 1 week) and let holography bring the antenna rms down to 0.25 mm. This new process promised a saving a total of approximately 5 weeks of antenna down time, human resources, and cost to the project if it were successful.

This new process was applied successfully for the first time at MDSCC on DSS-55 in July of 2003 (Table 8-1). Figures 8-22 and 8-23 are the holographically derived surface error maps of DSS-55 before (Fig. 8-22) and after (Fig. 8-23) holographically application showing the reduction of the antenna rms surface error from 0.90 mm to 0.25 mm presented on a ±0.73-mm color scale.

8.5.4 Subreflector Position Correction

The theory for the subreflector position correction via holography can be found in [14]. The subreflector position correction is derived from the low-order distortions in the antenna aperture phase function, which is derived from low-resolution holographic imaging (25×25 array for a 34-m antenna (or 51×51 for a 70-m antenna). Two low-resolution measurements are usually required due to the interaction of cubic and linear terms; the latter is due to systematic pointing errors. The time required for a single low-resolution measurement is approximately 45 minutes, and the data processing time is approximately 16 minutes.

Figure 8-24 shows the far-field amplitude pattern of DSS-24 as found in the initial stage of the holographic measurements. Corrections to the subreflector controller X, Y, and Z axis were applied as follows: 1.31 cm in the –X direction (The derivation of the subreflector correction in the X-axis is especially critical since no servo drive controller is available for this axis), 0.952 cm in the +Y direction, and 0.343 cm in the +Z direction resulting in the antenna far-field pattern shown in Fig. 8-25. From observing the antenna far-field pattern in these images, it is clear that the antenna went through a transformation from

unfocused to focused. The performance improvement obtained by setting the subreflector alone is 0.25 dB at X-band (8.45 GHz) and 3.6 dB at Ka-band (32 GHz).

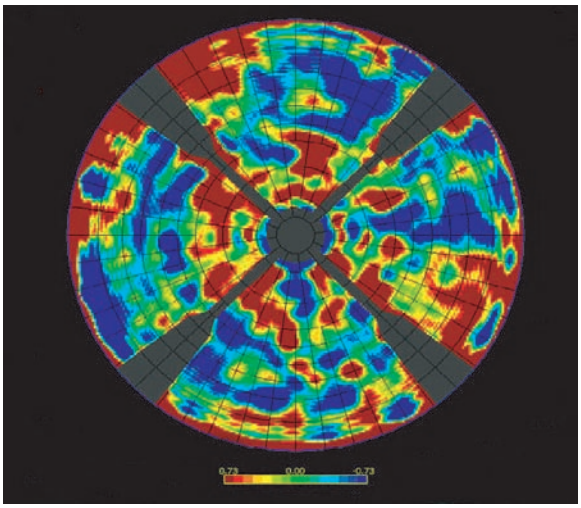

Fig. 8-22. DSS-55 surface error map before holography, 0.90-mm rms.

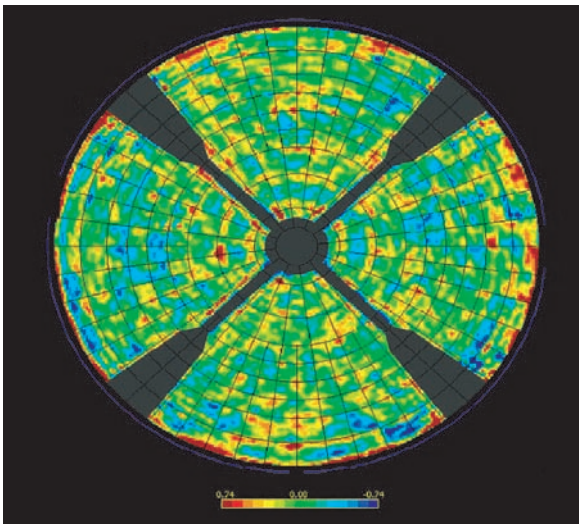

Fig. 8-23. DSS-55 surface error map after holography, 0.25-mm rms.

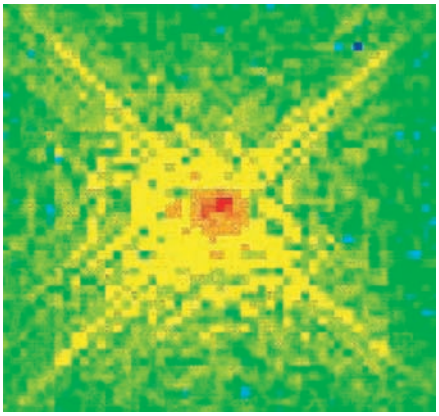

Fig. 8-24. DSS-24 far-field amplitude pattern before holographic corrections.

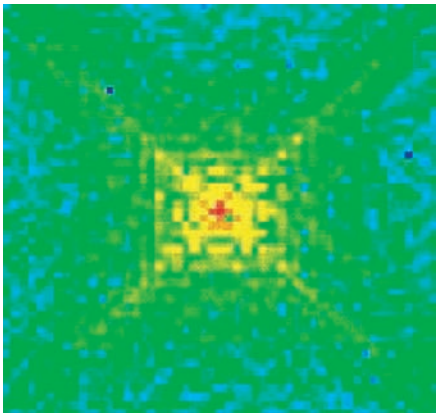

Fig. 8-25. DSS-24 far-field amplitude pattern after holographic corrections.

8.6 Conclusion

Microwave holography has proven to be an invaluable tool in the development and maintenance of large, high-performance ground antennas. The effective and highly successful application of microwave antenna holography to the large NASA–JPL DSN antennas has significantly improved their microwave and mechanical performance. For the 34-m BWG antenna subnet, the application of microwave antenna holography, combined with the implementation of low-noise system temperature of 22.3 K, resulted in a maximum *G/T* performance at Ka-band of 65.6 dB (on average and in vacuum) for each antenna at its rigging angle.

This improved performance has enabled new technologies and science advances. The added Ka-band observation frequency with the 34-m BWG subnet (which provided excellent amplitude and phase stability, high gain, and excellent blind pointing performances) enabled the highly successful Cassini radio science data return from Saturn ring occultation and bistatic radar. Another example is the high data rate achieved of 6 megabits per second (Mb/s) communicating with the Mars Reconnaissance Orbiter (MRO) while at a distance of 0.225 astronomical units (AU) using the 34-m BWG at Ka-band.

References

[1] J. C. Bennet, A. P. Anderson, P. A. McInnes, and A. J. T. Whitaker, "Microwave Holographic Metrology of Large Reflector Antennas," *IEEE Transactions on Antennas and Propagation*, vol. AP-24, pp. 295–303, 1976.

[2] P. F. Scott and M. Ryle, "A Rapid Method for Measuring the Figure of a Radio Telescope Reflector," *Royal Astronomical Society, Monthly Notices*, vol. 178, pp. 539–545, March 1977.

[3] M. P. Godwin, A. J. T. Whitaker, and A. P. Anderson, "Microwave Diagnostics of the Chilbolton 25M Antenna Using the OTS Satellite," *International Conference on Antennas and Propagation, 2nd, York, England, Proceedings*, Part 1, pp. 232–236, April 13–16,1981.

[4] D. J. Rochblatt and B. L. Seidel, "DSN Microwave Antenna Holography," *The Telecommunications and Data Acquisition Progress Report 42-76*, October–December 1983, pp. 27–42, February 15, 1984. http://ipnpr.jpl.nasa.gov/progress_report

[5] D. J. Rochblatt, Y. Rahmat-Samii, and J. H. Mumford, "DSN Microwave Antenna Holography Part II: Data Processing and Display of High-Resolution Effective Maps," *The Telecommunications and Data Acquisition Progress Report 42-87*, July–September 1986, Jet Propulsion Laboratory, Pasadena, California, pp. 92–97, 1986.
http://ipnpr.jpl.nasa.gov/progress_report

[6] C. E. Mayer, J. H. Davis, W. L. Peters, III, and W. J. Vogel, "A Holographic Surface Measurement of the Texas 4.9-m Antenna at 86.1 GHz," *IEEE Transactions On Instrumentation and Measurement*, vol. IM-32, pp. 102–109, 1983.

[7] O. M. Bucci, G. D'Elia, G. Franceschetti, and R. Pierri, "Efficient Computation of the Far Field of Parabolic Reflectors by Pseudo-Sampling Algorithm," *IEEE Transactions on Antennas and Propagation*, vol. AP-31, no. 6, pp. 931–937, November 1983.

[8] J. Ruze, "Antenna Tolerance Theory—A Review," *Proceedings of the IEEE*, vol. 54, no. 4, pp. 633–640, April 1966.

[9] D. J. Rochblatt, "Systems Analysis for DSN Microwave Antenna Holography," *The Telecommunications and Data Acquisition Progress Report 42-96*, October–December 1988, Jet Propulsion Laboratory, Pasadena, California, pp. 132–157, February 15, 1989. http://ipnpr.jpl.nasa.gov/progress_report

[10] D. J. Rochblatt and Y. Rahmat-Samii, "Effects of Measurement Errors on Microwave Antenna Holography," *IEEE Transactions on Antennas and Propagation*, vol. 39, no. 7, pp. 933–942, July 1991.

[11] D. Bathker, A. G. Cha, D. J. Rochblatt, B. L. Seidel, and S. D. Slobin, "70-meter Deep Space Network Antenna Upgrade Performance," *ISAP Japan 1989, Proceeding of the 1989 International Symposium on Antennas and Propagation*, Vol. 3, pp. 647–650, 1989.

[12] M. P. Godwin, M. F. Adams, P. J. Richards, E. P. Schoessow, and P. Wright, *Final Report on Ku-Band and X-Band Holographic Tests on the DSS-14 70-meter Antenna*, Eikontech Limited Report No A104 prepared for JPL, JPL D-40452, (internal document), Jet Propulsion Laboratory, Pasadena, California, October 1988.

[13] Y. Rahmat-Samii, "Microwave Holography of Large Reflector Antennas—Simulation Algorithms," *IEEE Transactions on Antennas and Propagation*, vol. AP-33, pp. 1194–1203, 1985 (see corrections, *IEEE Transactions on Antennas and Propagation*, vol. AP-34, p. 853, 1986.

[14] D. J. Rochblatt, "A Microwave Holography Methodology for Diagnostics and Performance Improvement for Large Reflector Antennas," *The Telecommunications and Data Acquisition Progress Report 42-108*, October–December 1991, Jet Propulsion Laboratory, Pasadena, California, pp. 235–252, February 15, 1992. http://ipnpr.jpl.nasa.gov/progress_report

[15] D. J. Rochblatt and B. L. Seidel, "Microwave Antenna Holography," *IEEE Transactions on Microwave Theory and Techniques*, Special Issue on Microwaves in Space, vol. 40, no. 6, pp. 1294–1300, June 1992.

[16] D. J. Rochblatt and B. L. Seidel, "Performance Improvement of DSS-13 34-Meter Beam-Waveguide Antenna Using the JPL Microwave Holography Methodology," *The Telecommunications and Data Acquisition Progress Report 42-108*, October–December 1991, Jet Propulsion Laboratory, Pasadena, California, pp. 253–270, February 15, 1992. http://ipnpr.jpl.nasa.gov/progress_report

[17] R. Levy, *Structural Engineering of Microwave Antennas: for Electrical, Mechanical, and Civil Engineering*, IEEE Antennas and Propagation Society, IEEE Press, New York, New York, 1996.

[18] D. J. Rochblatt, P. M. Withington, and H. J. Jackson, "DSS-24 Microwave Holography Measurements," *The Telecommunications and Data Acquisition Progress Report, No. 42-121*, January–March 1995, Jet Propulsion Laboratory, Pasadena, California, pp. 252–270, May 15, 1995. http://ipnpr.jpl.nasa.gov/progress_report

[19] D. J. Rochblatt, P. M. Withington, and H. J. Jackson, "DSS-24 Antenna RF Performance Measurements," *Microwave Holography Measurements*, 890-270 JPL D-12277, (internal document), Jet Propulsion Laboratory, California Institute of Technology, Pasadena, California 890-270: pp. 2-1 to 2-18, February 1, 1995.